Analysis and interpretation of three composite VHE gamma-ray sources

Bachelor Thesis in Physics

Submitted by

Darius Grüber

04.08.2022

Erlangen center for astroparticle physics (ECAP)
Friedrich-Alexander-Universität Erlangen-Nürnberg

Supervisor: Dr. Alison Mitchell

Contents

Abstract

This thesis can be seen as a detailed analysis of sources already firmly presented in the Hess galactic plane survey (HGPS), which was done by the H.E.S.S. colaboration in 2018. The data which will be used was taken by the H.E.S.S. telescope array, which is stationed in Namibia. The main sources observed and analysed are HESS J1119-614, HESS J1833-105 and HESS J1846-029. All three systems contain a Supernova remnant (SNR) and a Pulsar Wind Nebula (PWN). A spatial and spectral analysis as well as a discussion about the categorisation of the three systems will be held. The final categorisation will take the conversion efficiency $\epsilon_{1-10\text{TeV}}$ as well as hadronic and leptonic models into account. Furthermore additional data from radio and X-ray observations will be included, in order to describe the broad band spectral properties of the sources.

1 Theoretical Properties

1.1 Supernova Remnants

Once the fusion process in a star uses heavier elements than hydrogen or helium the stars lifetime is about to come to an end. Massive stars continue their fusion processes until they reach the element iron in their interaction chain. Once this level is reached a star can no longer produce energy with fusion. The reason for this is that the resulting energy from an iron fusion would be higher than the one put into the reaction [1].
Without fusion inside the star the binding energy decreases such that a collapse due to gravitational forces seems to become unavoidable. However during this phase the protons and electrons are pushed together such that an interaction between them occurs. During this scattering process a neutron and a electron neutrino are produced. This in total produces a neutron degenerate pressure which counteracts the gravitational pull. The outer material now interacts with this inner core until a massive amount of about $\sim 10^{50}$erg of potential neutron energy is released. The former outer layers are now injected into the interstellar medium [1]. If the former mass of the star is about 5-12$M_\odot$ a neutron star will be left after the Supernova. One now speaks of a pulsar if the new born neutron star rotates. However if the dying star has a too large mass the gravitational force is too strong and a black hole comes into existence [1].
The other possible mechanism in which a Supernova can occur is, if a white dwarf pulls material from a red giant in its nearby region. This results in an ongoing material flow towards the white dwarf until it collapses because it passed the Chandrasekar limit. At this point the gravitational forces cause the collapse of the dwarf. This increases the temperature inside such that carbon and oxygen start to fuse which results in a cascade of nuclear interactions releasing an energy of up to $\sim 10^{52}$erg [1].
As already mentioned above a possible resulting neutron star can be a pulsar. This object has two significant characteristics, one being that a pulsar spins around itself at very high speed and second having very high magnetic fields. These two properties are the reason why pulsars eject high energy particles. The surrounding enviroment of a pulsar can be contained by charged particles, which form a nebula around the pulsar, also called pulsar wind nebula (PWN) [9].
Sometimes a differentiation between the SNR and PWN (which contains also the pulsar

itself) can not be made. If this is the case one speaks of the corresponding source to be a composite system. An example for composite systems are the later discussed sources HESS J1119-614, HESS J1833-105 and HESS J1846-029.

1.2 Particle interactions

As already mentioned above, pulsars have high magnetic fields, which makes them large particle accelerators. Also due to the high magnetic field an electric field is induced which generates electrons and positrons by pair production in the magnetosphere [[2], p.2]. Besddies that the particle wind from the pulsar can now interact with the ambient medium remaining from the Supernova. A resulting synchrotron emission can be seen in the radio to gamma-ray energy range [[3],p.1]. Synchrotron emission occurs, when charged particles travel in a curved path caused by a magnetic field, which interacts with the particles [4]. In this case the magnetic field of the pulsar is responsible for this deflected particle curve. The charged electrons and positrons from this accelaration process can now produce gamma-rays via pair production. Furthermore inverse compton (IC) scattering can be seen in the shock region. Unlike normal compton scattering, where a photon looses its energy during the scattering process, in the inverse case a photon gains energy through this interaction [5]. IC interactions can be seen in the X-ray to gamma-ray energy range. They are the main interaction process which will be later looked at concerning leptonic interactions. Yet additionally the effect of bremsstrahlung is also taken into account. This interaction process can be described as a acceleration or deceleration process which is either do to a surrounding magnetic field or particles which interact with the electromagnetic radiation [6]. In this case we will look at bremsstrahlung interactions in the ambient medium of the SNR. During the bremsstrahlung interactions gamma-rays can be produced either if an electron and a positron undergo a pair-production or other leptons (e.g. $\mu^{\pm}$) interact with each other and their resulting interaction products undergo pair-production.

However as the SNR surrounds the PWN also hadronic interactions need to be looked at. In this case the main hadronic interaction which will be considered is the proton-proton scattering in the ambient medium. When protons collide with each other it is possible that pions are produced, which then decay into photons [7]. One could also split the hadronic interaction into several subinteractions (e.g. taking pion interactions seperately into account). However as the gamma-rays comming from hadronic interactions are either due to direct pion decay or the resulting pion decay of a proton-proton collision, it is decided to take only the later case into account.

Later the measured spectral energy distribution (SED) will be looked at, where the above mentioned particle interaction processes will be taken into account. Usually prefering the hadronic loss model for the injected particle spectrum implies a SNR origin of the gamma-ray emission. This is due to the particle kind which populates the SNR, as there mainly occur hadronic interactions.

For the PWN one expects leptonic emission to be comming from the above mentioned mechanisms, as the PWN and the contained pulsar mainly emit electrons and positrons. The pulsar accelerates electrons/positrons along its magnetic field until the particles travel with almost the speed of light. They then drift in a wave front away from the pulsar itself and undergo pair production, which can be measured.

If both interaction models are reasonable within error assumptions one categorises the source

as being of a composite SNR and PWN kind.

1.3 The H.E.S.S. telescope array

The High Energy Stereoscopic System (H.E.S.S.) consists of five imaging atmospheric Cherenkov telescopes (IACT) to detect gamma-ray showers by astronomical sources [8]. However the data which will be analysed in this work was taken mainly in phase one of the telescope array, hence the reason why only data with four telescopes is taken. In order to detect a gamma-ray shower from a intergalactic source the main operational technique to be used is the IACT. When high energy gamma-rays interact with our atmosphere an air shower of secondary particles will be produced [8]. These secondary particles travel faster than the speed of light, i.e. they produce Cherenkov light.

The light usually is distributed in a circular shape with a radius of ~125m on the ground. It shows that for one primary photon with an estimated energy of 10^{12}eV only about 100 $^{\text{photons}}/_{\text{m}^2}$ reach the ground [8]. If a telescope happens to be in this target circle and if enough photons hit the telescope a track image of the air shower can be seen [8]. As already mentioned above, four telescope were in use during the data acquisition time. These telescopes have a diameter of 12m with a focal lenght of 15m and a reflectivity of >80% [8]. The cameras used to capture the events are CCDs with an 8-stage photomultiplier (PMT) tube behind them [8]. A trigger inside the camera only records a signal if 3 to 5 coincidential signals in overlapping 8x8 pixel sectors occur [8]. In general however a signal is only counted if more than one telescope sends a trigger message to a central station. This is the reason why only datasets with at least three telescopes in use will be looked at [8].

One issue however with a ground based telescope array is that the quality of the acquired data partially depends on the weather. This means that in cloudy skies or if dust lies on telescopes, the observed counts measured by an IACT is reduced. However, these weather effects will not significantly reduce the observational data, so these effects can be neglected.

2 Data structure & Data handling

The datasets which will be handled are in the standard *FITS* format, as it is usual for H.E.S.S. data and IACT data in general. Furthermore this research made use of gammapy[1], a community-developed core Python package for TeV gamma-ray astronomy [12]. The version used in this case is the currently most up to date version gammapy-0.20[2] [see [13]].

2.1 Instrument response function

The corresponding data is stored in observation classes, which are defined as times where the so called instrument response function (IRF) is stable [10]. IRF's are important if one wants to reproduce the expected number of events N(p,E). The following explanation of the IRF used can be seen in [11].

An IRF $R(p,E|p_{\text{true}}, E_{\text{true}})$ is used to solve the integral

$$N(p, E)\, dp\, dE = t_{\text{obs}} \int_{E_{\text{true}}} dE_{\text{true}} \int_{p_{\text{true}}} dp_{\text{true}} R(p, E|p_{\text{true}}, E_{\text{true}}) \cdot \Phi(p_{\text{true}}, E_{\text{true}}), \quad (1)$$

where $\Phi(p_{\text{true}}, E_{\text{true}})$ is the sky flux model and t_{obs} is the observation time.

In this case the IRF will be a product of three functions in such a way that

$$R(p, E|p_{\text{true}}, E_{\text{true}}) = A_{\text{eff}}(p_{\text{true}}, E_{\text{true}}) \cdot \text{PSF}(p|p_{\text{true}}, E_{\text{true}}) \cdot E_{\text{disp}}(E|p_{\text{true}}, E_{\text{true}}). \quad (2)$$

$A_{\text{eff}}(p_{\text{true}}, E_{\text{true}})$ represents the effective area of the detector, usually given in [m^2]. It is mostly defined as

$$A_{\text{eff}}(p_{\text{true}}, E_{\text{true}}) = A \cdot \eta(p_{\text{true}}, E_{\text{true}}), \quad (3)$$

where A is the detector area and $\eta(p_{\text{true}}, E_{\text{true}})$ is the detection efficiency at true position and energy values p_{true} and E_{true}.

The point spread function (PSF) denotes the probability of measuring the position p if the true direction and energy is p_{true} and E_{true}. The most commonly used unit for the PSF is sr^{-1}, which can differ for other PSF formats.

The last component of the IRF is the so called energy dispersion $E_{\text{disp}}(E|p_{\text{true}}, E_{\text{true}})$, which gives the probability that an energy E is measured when true direction and energy is p_{true} and E_{true}. The energy dispersion is given in units of TeV^{-1}.

All three functions can be dependent on each other and are obtained by Monte-Carlo simulations. In the datasets which will be used in this thesis all IRF's are already stored in the *FITS* files, such that these simulations will not be observed here. Also they would go beyond the scope of this thesis.

---

[1] https://www.gammapy.org
[2] https://zenodo.org/record/6552377

2.2 Background reduction

The background reduction is split into two subsets, in the first part the field of view (FOV) in a region of 2° around the center of each observation will be looked at. In the second part the source energy range and a threshold will be set for the data. Given that only high energy gamma-ray sources shall be observed, an energy range of 0.1-100 TeV is chosen. These two criteria will then be used to stack all observations together in order to get a single dataset, which will be used for further analysis.

2.2.1 Field of view

In order to only obtain data from the dedicated sources a background reduction needs to be applied on the datasets. In this case for HESS J1119-614 a FOV of 4°×4° with a bin size of 0.02 is to be taken, whereas for HESS J1833-105 and HESS J1846-029 a FOV of 2°×2° with a bin size of 0.01 is chosen. The reason for this decision is that HESS J1119-614 turns out to be larger, such that a wider FOV is necessary. However in all three cases a maximum offset radius of 2° is to be chosen, because this ensures that no data in the surrounding area of the sources is cut out. Furthermore the data taken by H.E.S.S. has two possible data cuts which will be examined. These being the so-called standard and hard cut data. The difference between them is that the hard cut is in general more conservative concerning selection cuts. Applying hard cuts lets one only keep the best candidate gamma-ray events, they are also more optimized for higher energies. However standard cuts generally allow one to use more data counts, sucht that they are also viable for analysis purpose. In addition to the standard and hard cut selection options, additional exclusion zones are included to the datasets. In order to model a FOV background with no sources in it, all known sources around the center in a radius of 5° are excluded (this also includes the pulsars which shall be observed). However one could argue that even though an exclusion of all known sources will not be sufficient in the case of a low energy hotspot or source near the desired regions. In order to further exclude background source emission, a second cut concerning the energy will be applied.

2.2.2 Energy

In order to select only energies belonging to the dedicated source, two energy values will be taken into account. These are the energy bias which takes the energy dispersion E_{disp} into account and the lower energy threshold determined by the effective area A_{eff}. Those values will be (like the FOV backround reduction) obtained for each individual observation run. The energy dispersion E_{disp} will be obtained with a bias tolerance of 10% for energies between 0.1-100 TeV. The lower energy threshold is taken in the same range as the energy dispersion is taken, however it also takes the FOV into account. For every run the bias and threshold will be compared and only the bigger value will be taken. By doing this it is ensured that only valid energies are to be taken into account. Also there is a difference between hard and standard cut after applying the energy cut. This being that hard cut data tends to have a higher energy threshold than standard cut data. Figure 1 shows the threshold against the zenith angle in a general case. For this thesis only data below 65° will be taken into account, which is the highest possible angle to be looked at by H.E.S.S.. However as one sees later, the observed sources will be well below this limt.
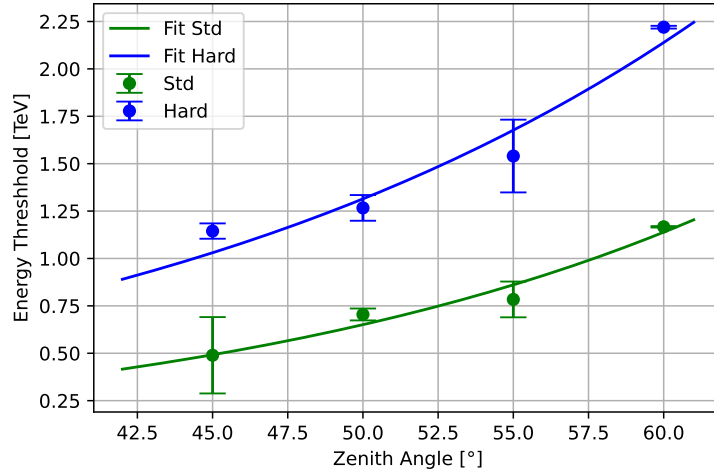
Figure 1: Comparison of standard and hard cut data for different zenith angles. The datapoints were obtained from different observation runs of the crab nebula. The fit functions are just simple exponential functions only plotted to show the effect of the cuts.

One can see that the hard cut has higher energy thresholds than the standard cut. This however must not be the case in every measurement. It can rather be seen as a guide on how to judge standard and hard cut in terms of their background energy. It turned out that this has almost no influence on the outcoming flux points of the observed sources.

3 Methods

This section will deal with the methods and models used to analyse the sources. For all sources a background reduction like described in section 2.2 is done. After this several models will be set on the stacked counts datasets which remain after the reduction.

3.1 Spatial Analysis

In order to describe the sources a spatial and a spectral model as well as a background spectral model are set on the datasets. In order to describe the spatial dimensions of the source, a gaussian spatial model is set uppon the datasets. The spatial model is of the form

$$\phi(\text{lon}, \text{lat}) = \frac{1}{2\pi\sigma^2} \cdot \exp\left(-\frac{1}{2}\frac{\theta^2}{\sigma^2}\right), \tag{4}$$

where (lon,lat) is the location of the expected source, θ is the sky separation to the model center and σ^2 the variance. Size assumptions of the analysed sources will be done with the value of σ. If a source is of a circular shape, its width is of the same size as its height. Taking this into account the source has an approximate size[3] of

$$\sigma_{\text{source}} := \sigma_h = 2 \cdot x_\sigma \cdot \sigma, \tag{5}$$

where σ_h is the source height. The position error is then given as

$$\Delta\sigma_{\text{source}} = \sqrt{\left(\frac{\partial\sigma_{\text{source}}}{\partial\sigma}\right)^2 \cdot (\Delta\sigma)^2} = 2x_\sigma \cdot \Delta\sigma. \tag{6}$$

In this case x_σ=1.5 in order to contain 68% of the counts then 2D gaussian fit is done. Considering size limits discussions done by [[16], p.15], a systematic error on the source size can not be left out of the discussion, such that a minimum source size of σ_{syst}=0.03° is set. Therefore this lower limit needs to be applied if the equation

$$\sigma_{\text{source}} - 2\Delta\sigma_{\text{source}} > \sigma_{\text{syst}} \tag{7}$$

does not hold. Should this be the case an upper limit on the source size will be applied, which is defined as

$$\sigma_{\text{UL}} = \max(\sigma_{\text{syst}}, \sigma_{\text{source}} + 2\Delta\sigma_{\text{source}}). \tag{8}$$

Every source which violates equation 7 can be treated as being point like and the upper limit σ_{UL} can be applied as the highest estimated source size.

3.2 Spectral Analysis

Besides a spatial model two different spectral models are selected to describe the flux of the sources. At first a simple power law of the form

$$\phi(E) = \phi_0 \cdot \left(\frac{E}{E_0}\right)^{-\Gamma} \tag{9}$$

---

[3]The formula equates to the method used by gammapy, as one can look up the source code on the documentation site [25].

will be fitted on the dataset. In this case ϕ_0 is the amplitude, E the energy, Γ the spectral index and E_0 the reference energy, which has a frozen value of 1TeV during the fitting process. In addition, an exponential cutoff power law is fitted in another fitting process. This spectral model is of the form

$$\phi(E) = \phi_0 \cdot \left(\frac{E}{E_0}\right)^{-\Gamma} \cdot \exp(-(\lambda E)^{\alpha}), \tag{10}$$

where ϕ, E, Γ, E_0 have the same meaning as in equation 9, but additionally a cutoff paramater λ and a second index α are introduced. The spectral background model used is of the same shape as the power law like in equation 9 only with a normalized amplitude. The background model has always the amplitude 1 and an index 0.

After the models are set on the datasets, corresponding flux points of the sources will be estimated between 0.1-30TeV. A similar method as described in the HGPS (see, e.g., Sect. 4.11 in [16]) is used to derive the flux points from the models given by the equations 9 & 10. For every source a total number of 8 bins is selected for the reconstructed energy in a logarithmic scale from starting energy E_1=0.1TeV to E_2=30TeV. The upper limit is selected as 30TeV, because for higher energies the residuals of the flux points-model tend to be too high.

3.2.1 Spectral properties

After the most optimal model is chosen, the Luminosity L_γ and spin-down luminosity $\dot{E}$ are calculated. Luminosity is calculated like explained in [[17], p.5f.], using the formula

$$L_\gamma = 1.92 \cdot 10^{44} \frac{I_{>1\text{TeV}}}{\text{cm}^{-2}\text{s}^{-1}} \cdot \frac{\Gamma - 1}{\Gamma - 2}(1 - 10^{2-\Gamma}) \cdot \left(\frac{d}{kpc}\right)^2 \text{ergs}^{-1} \tag{11}$$

for the luminosity between 1-10TeV. In this case $I_{>1\text{TeV}}$ is the integral flux above 1TeV, Γ the index of the power law chosen and d the distance to the source in kpc. The error is calculated with the formula

$$(\Delta L_\gamma)^2 = \left(\frac{\partial L_\gamma}{\partial I_{>1\text{TeV}}}\right)^2 \cdot (\Delta I_{>1\text{TeV}})^2 + \left(\frac{\partial L_\gamma}{\partial \Gamma}\right)^2 \cdot (\Delta \Gamma)^2 \tag{12a}$$

$$= L_\gamma^2 \cdot \left[\left(\frac{\Delta L_\gamma}{I_{>1\text{TeV}}}\right)^2 + \left(\frac{\ln(10)}{1 - 10^{\Gamma-1}} + \frac{1}{(\Gamma - 2)(\Gamma - 1)}\right)^2\right]^2, \tag{12b}$$

where $\Delta I_{>1\text{TeV}}$ is the error of the integral and $\Delta\Gamma$ the index error. Considering discussions from [[17], p.6], a distance error can be neglected, as it is not likely to be gaussian distributed. Furthermore taking [[17], p.10] into account, the spin-down luminosity $\dot{E}$ is defined as

$$\dot{E} = \dot{E}_0 \cdot \left(1 + \frac{t}{\tau_0}\right)^{-\frac{n+1}{n-1}}, \tag{13}$$

with $\dot{E}_0$ the initial spin-down luminosity, t the time, $\tau_0 = 10^{2.5-3.5}$yr and the braking index n. In addition it is possible to compute the pulsar energy by integrating equation 13, resulting in the energy at time t to be

$$E(t) = \int_0^t \dot{E}(t')dt' = \dot{E}_0 \int_0^t \left(1 + \frac{t}{\tau_0}\right)^{-\frac{n+1}{n-1}} dt' = \dot{E}_0 \tau_0 \frac{1-n}{2}\left[\left(1 + \frac{t}{\tau_0}\right)^{\frac{2}{1-n}} - 1\right]. \tag{14}$$

$\dot{E}_0$ can be calculated by inverting equation 13 and using a literature value for $\dot{E}$. However for most sources no braking index is defined, such that in these cases n = 3 will be chosen. Another important size which can be calculated is the conversion efficieny of the pulsars rotational energy to gamma-rays. Considering discussions made by [[18], p.4], the formula

$$\epsilon_{1-10\text{TeV}} = \frac{L_\gamma}{\dot{E}} \tag{15}$$

is chosen to calculate the efficiency.

3.2.2 Spectral energy distribution

At last a SED with the loss interactions discussed in section 1.2 will be set upon the flux points. The aim of this application is to determine whether the observed gamma-rays are produced by hadronic or leptonic interaction processes. The hadronic particle injection spectrum is in this case a power law of the form

$$\varphi(E) = \varphi_0 \cdot \exp(-\alpha), \tag{16}$$

where α is the index and φ_0 is the amplitude, which is normalized through

$$\varphi_0 = E_{\text{tot}} \cdot \left(\int_{E_0}^{E_1} \varphi(E) \cdot E \, dE \right)^{-1}. \tag{17}$$

E_{tot} is the total energy injected into the spectrum and E_0 and E_1 are the edges of energy the power law shall be computed. The reason for taking a power law injection spectrum is that hadronic processes are predicted to come from the shock acceleration.

For the leptonic particle injection a logarithmic parabola law is taken, because leptons are expected to be coming from a more continuous injection process. This spectral model is more suitable, when one wants to model particles where energy losses and source evolution play a bigger role. This makes it more suitable for describing electrons, as they are expected to be injected in continuous waves from the PWN. The formula used for the logarithmic parabola law is

$$\varphi(E) = \varphi_0 \left(\frac{E}{E_{\text{ref}}} \right)^{-\left(\alpha + \beta \cdot \log\left(\frac{E}{E_{\text{ref}}} \right) \right)}, \tag{18}$$

where φ_0 is computed like before, E_{ref}=1TeV and α, β are indices. The particle flux model with losses is in this case defined by a partial differential equation of the form

$$\frac{\partial N}{\partial t} = Q(E,t) - \frac{\partial}{\partial E}(b(E,t) \cdot N(E,t)) - \frac{N(E,t)}{t_{esc}(E,t)}, \tag{19}$$

taken from [[15], p.259]. In this case Q(E,t) is the spectrum of particles injected into a system, b(E,t) is the energy loss rate of the injected particles, $t_{esc}(E,t)$ is the timescale for the particle escape and N(E,t) the total resulting spectrum at a given time. In order to get SEDs from this particle loss equation the python package GAMERA[4] is used. It is a project launched by the Max Planck Intstitute for Nuclear Physics in Heidelberg (MPIK), which handles the spectral modelling of non-thermally emitting astrophysical sources in a simple

---

[4]`https://github.com/libgamera/GAMERA`

and modular way (see also [19]). With this package an analytic solution (see [[15], p.260f.]) for time constant b and t_{esc} will be computed in order to decide which particle population model currently prevails. The loss interactions that will be taken into account are synchroton radiation, proton-proton interactions IC scattering and bremsstrahlung. The proton-proton interaction depends on the power law and ambient density in the SNR medium. Synchrotron radiation depends on the magnetic field set on the model. For inverse compton scattering a thermal target photon field inside the PWN and a radiation field as described by [27] is set. The photon field thermal target field depends on the temperature and energy density around the SNR. Furthermore the bremstrahlung used depends also on the ambient density. The models for proton-proton interaction and IC scattering will be computed for the calculated data only. The method which will be used to find a model is a 5% significance χ^2 test. After the model fits the data in the computed energy range, extra data from other experiments and papers (where possible) will be included. There also the synchrotron radiation will be set onto the extra data.

4 Results

This chapter contains the results after background reduction (section 2) and model fitting (section 3) steps are applied to the datasets. Each source will be individually handled and discussed. For each source standard and hard cut were analysed seperately and only one cut is chosen and presented. For this cut the simple power law and exponential cutoff power law fit will be discussed. In addition the sky map of the best fitting spectral model will be shown. For the last analysis step this best fit model will be used, in order to find the best fitting particle loss model given by equation 19.

4.1 HESS J1119-614

The first source to be looked at is the composite system HESS J1119-614, which has a magnetic surface field of $4.1 \cdot 10^{13}$G, a spin-down Luminosity $\dot{E} = 2.3 \cdot 10^{36}$ergs^{-1} and is located at a distance of d=(8.4±0.4)kpc [[16], p.33]. The observations used in this case were taken at a mean zenith angle of 39.97° with a mean offset angle of 1.36°. The total live time is 81.46hrs and a total number of 176 observations are considered in the analysis, with each observation run having a live time of 28min. A histrogram of the zenith angle as well as the offset angle can be seen in figure 2.
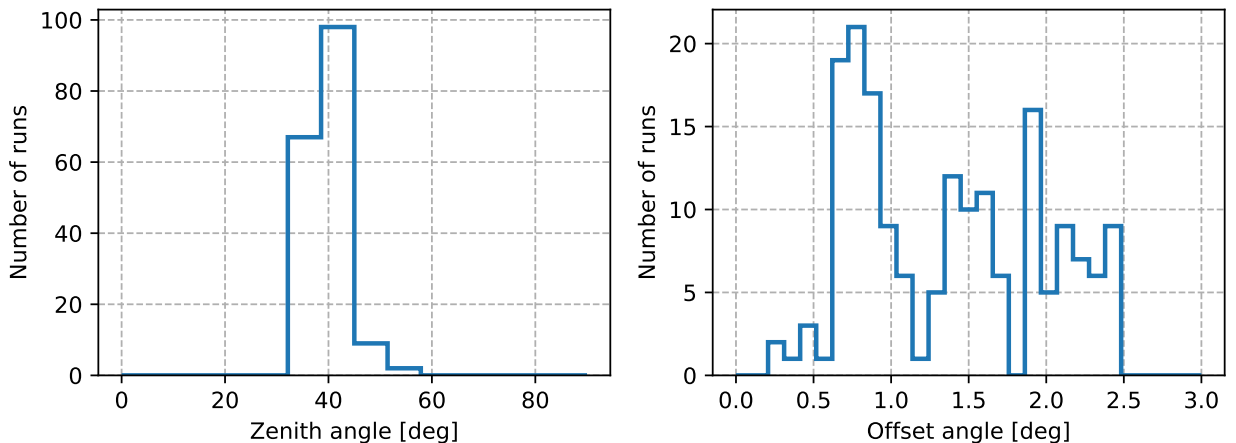

Figure 2: Histogram of the zenith angle and the corresponding offset histogram for HESS J1119-614.

The distribution of zenith and offset angle is the same for standard and hard cut. For this source it is decided to use the standard cut for further analysis as it shows that in both cases almost the same fit values occur. However as there are more counts included for standard cut data it is more valid to use it in this case.

4.1.1 Data analysis & Modeling

After the background reduction to only one stacked dataset, it is found that 185582.16 counts belong to the background, whereas only 1265.84 belong to the source. This results in a signal

to background ratio of 0.68%. The reduction is done as explained in section 2.2 with an average energy threshold of (0.46±0.11)TeV. Figure 3 shows the significance histogram of the source, where the off bins are the counts which are excluded in the background reduction. As one can see, a typical normal distribution occurs in this case, which means that the background reduction has not cut out relevant source data.
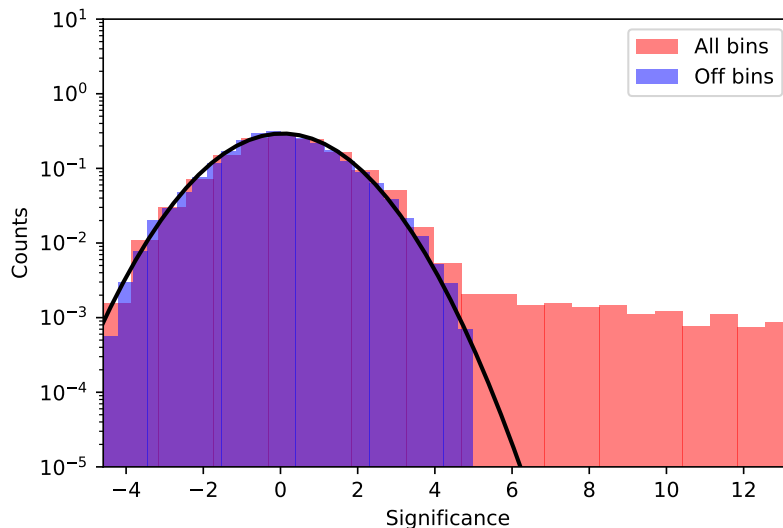

Figure 3: Histogramm of the significance for the background estimation with the blue graph belonging to the source. The normal distribution shape of the source histogram shows that no source related data is cut out.

Power Law Fit

The resulting fit parameters for the power law fit can be seen in table 1. The spatial model is of a circular shape (see figure 6), hence the reason an approximation as a circle is viable in this case, resulting in a diameter of (0.30± 0.06)°. The computed flux points with this model set can be seen in figure 4.

From the obtained flux model the estimated flux in Crab units is (5.0±0.7)%. All data used

type	parameter	value	unit
spatial	R.A. (J2000)	169.72 ±0.03	deg
spatial	Dec. (J2000)	-61.45 ± 0.02	deg
spatial	σ	0.10 ± 0.02	deg
spectral	ϕ	(1.56± 0.16)·10^{-12}	$TeV^{-1}cm^{-2}s^{-1}$
spectral	Γ	2.58 ± 0.09	

Table 1: Fit values for the power law fit with errors.

for Crab comparsion calculations is taken from the Crab H.E.S.S. catalog by [29].
A comparsion with the HGPS data and their computed power law can be seen in figure 5. All data used from HGPS is from their catalog which is avaiable as a *FITS* file on the HGPS
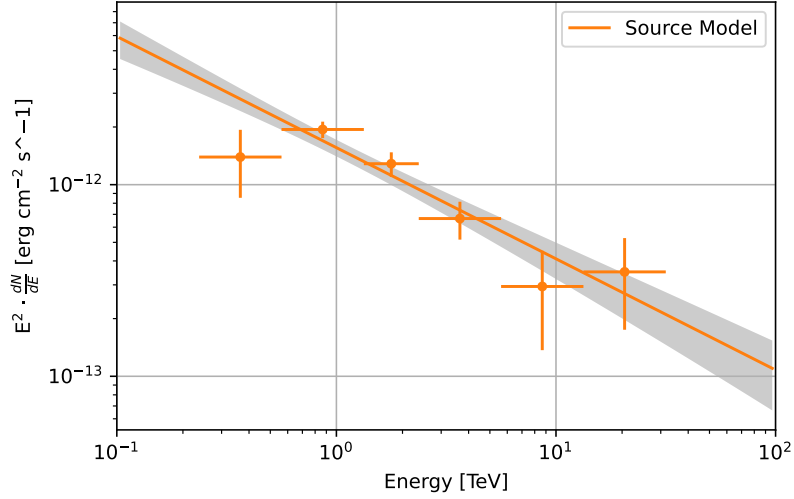
Figure 4: Flux points estimated for HESS J1119-614, note that the energy, the flux dN/dE is multiplied with, is given in the unit erg, as this is the usual energy unit in high energy astroparticle physics.
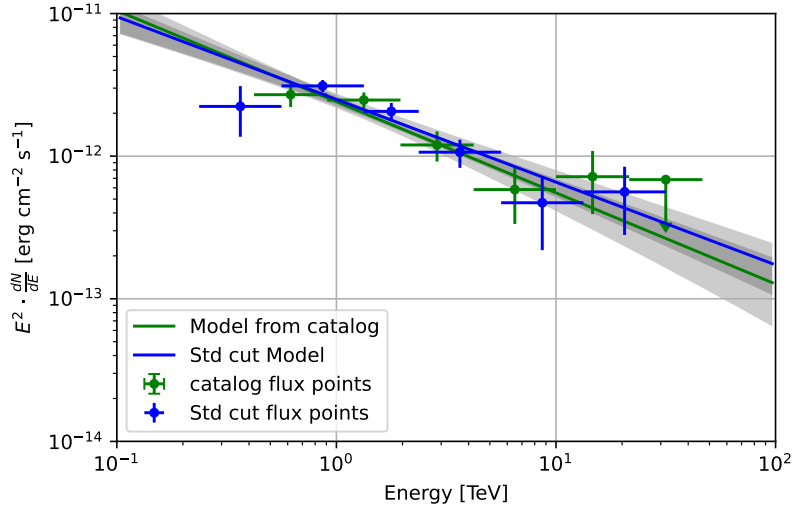
webpage[5].

Figure 5: Comparison plot of the calculated flux points with the extracted HGPS flux point data.

As one can see the calculated flux points from the fit done in this work is consistent with the HGPS. However one needs to take into account that the flux points are only viable till 30TeV, whereas the flux points from the HGPS were calcuted for energies up to 50TeV [[16], p.27]. The obtained gamma-ray map can be seen in figure 6, where also the $\sqrt{TS}$ ($\approx$ Significance) is shown. The correlation radius is set to 0.15°, it determines the size of the region around

---

[5] https://www.mpi-hd.mpg.de/hfm/HESS/hgps/

center to compute $\sqrt{TS}$. Negative $\sqrt{TS}$ can occur when the background is overestimated, as described in [23]. The FOV of the image is (1.5°×1.5°) and the 70% containment radius is in this case set to 0.15°. The reason for this is that as one can see in figure 6, the containment radius obtained from the PSF of the observed energy band is mostly below 0.15°. Values below will not be taken into account because they have a lower significance. Therefore if the observed containment radius at 1σ is below 0.15°, it is set to 0.15°. Also the 2σ containtment radius is plotted, which contains 95% of the counts measured. One can also see in 6 that the radio and gamma-ray emission have a different center location than the estimated model center. The centers however have a low difference to each other, such that with errors taken into account, no significant difference between the positions occur.
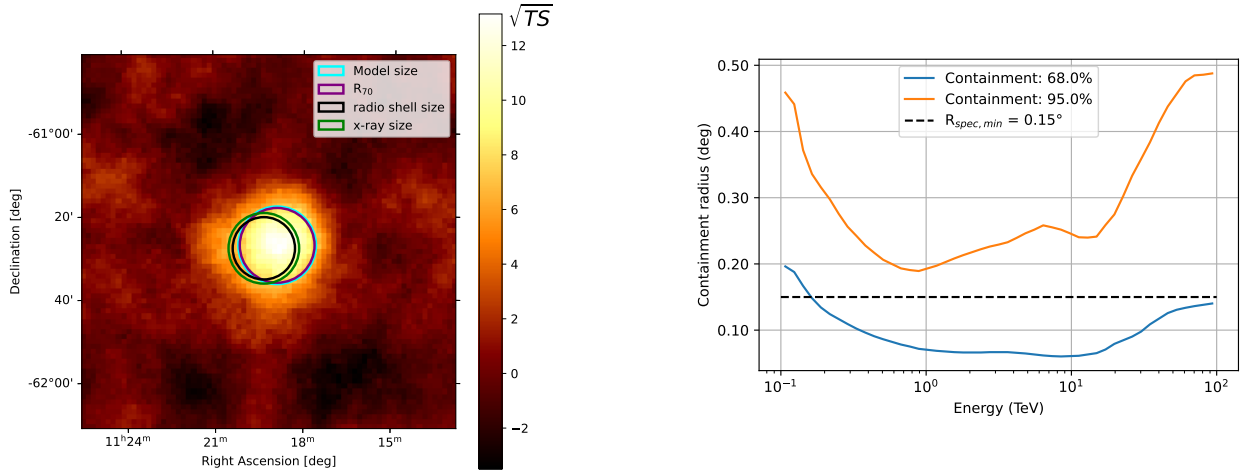

Figure 6: Very high energy (VHE) gamma ray image (left) for HESS J1119-614 with the associated model size and 70% containment radius for the power law fit. The radio and gamma-ray size are taken from [[20], p.1]. Additionally the containment radius (right) for 1 and 2 σ is plotted, the black doted line indicates the 0.15° cut.

Exponential Cutoff Power Law Fit

The fit data can be seen in table 2 with a resulting flux is (2.2±0.7)% of Crab nebula. However the flux is only calculated for fluxpoints between 0.1-20TeV, as the model is not reliable enough for energies above 20TeV. Again the spatial model is of a circular shape which makes it possible, that equation 5 can be applied. This results in a size of (0.33 ±0.03)°. This is comparable to the already obtained model parameters from the power law fit. A bigger difference between both models can be seen if one looks upon the comparison of the calculated data with the HGPS data. Figure 7 shows both calculated and HGPS flux point datasets, which in this case differ concerning the shape of the model. This however lies in the nature of the fits, as in this case a comparison between an exponential cutoff and a simple power law is done. Considering only the flux points, different models make no difference such that a reasonable difference between calculated and HGPS data points can be observed.
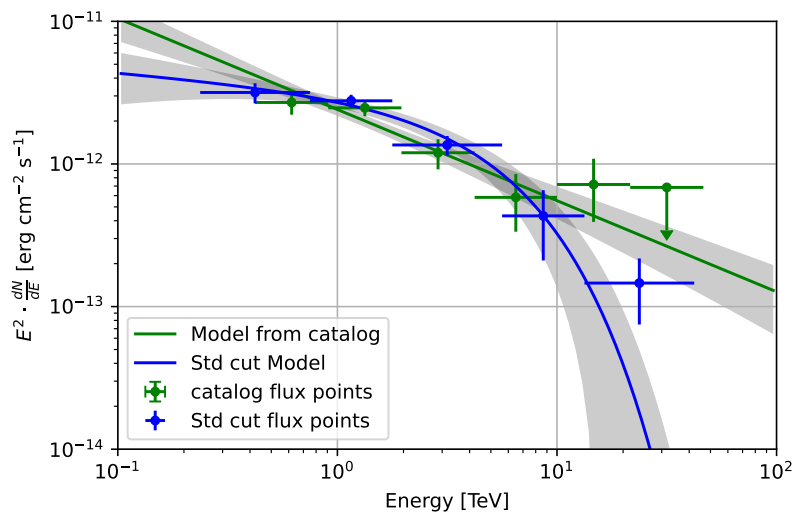

Figure 7: Calculated and HGPS flux points with the selfsame HGPS data as in figure 5. Note that the calculated exponential cutoff flux model has a very high difference to the HGPS model for energies above 30TeV.

Although the exponential cutoff power law describes the flux reasonably for lower energies, it

type	parameter	value	unit
spatial	R.A. (J2000)	169.73 ± 0.03	deg
spatial	Dec. (J2000)	-61.46 ± 0.02	deg
spatial	σ	0.11 ± 0.01	deg
spectral	ϕ	(2.06± 0.26)·10^{-12}	$TeV^{-1}cm^{-2}s^{-1}$
spectral	Γ	2,13 ± 0.20	
spectral	λ	0.20 ± 0.10	TeV^{-1}
spectral	α	1.00 ± 0.00	

Table 2: Fit values for exponential cutoff power law fit with errors.

has problems doing so with higher energy values. One can see that by counting the obtained

data points in this case, as here only 5 flux points could be estimated, compared to the 6 from the earlier power law fit. This indicates that the favourable spectral model for the standard cut will be the power law and not the exponential cutoff law. The obtained gamma-ray image has no visible difference to the already shown power law image and is thereby not shown.

4.1.2 Interpretation

When reagarding the power law fit and the exponential cutoff fit, it is clearly, that the power law is the preferable model to use. The reason for this is that the power law covers a larger energy range making it more usable. In addition the power law flux points have the highest mean $\sqrt{TS}$ value, which is 5.19. The exponential cutoff $\sqrt{TS}$ value is below 5, such that this model can be ruled out.

With the power law model set, the Luminosity $L_\gamma(1-10\text{TeV}) = (2.61\pm0.3)\cdot10^{-34}(d/8.4\text{kpc})^2$ ergs^{-1} is computed. This makes up an efficiency of $\epsilon_{1-10\text{TeV}} = L_\gamma/\dot{E} = 1.1\%$, which confirms the value [16] has calculated. Furthermore this makes the efficiency belonging to the $<10\%$ efficiency range, in which PWN's are found [18]. Using equation 14 for the pulsar energy, E(t)=$3.43\cdot10^{48}$ erg is calculated, where for this pulsar the rare case of a known braking index occurs, being n=2.684$\pm$0.002 [[16], p.33]. Furthermore as the age is estimated to be between 4.2-7.1kyr [see [16], p.33] and τ_0 being somewhere between $10^{2.5-3.5}$yr, the mean age of 5.65kyr and $\tau_0 = 1$kyr are taken to calculate the pulsar energy.

Next a time constant SED will be computed as described in section 3. For the hadronic model $\chi^2 = 1.24$ and for lepton model $\chi^2 = 4.24$ are computed, which are below the critical value of 11.070 for 5 d.o.f. [26]. Both models thereby describe the calculated flux points within the model assumptions. Figures 8 & 9 show both the hadronic and leptonic case, the parameters used can be seen in table 3 & 4. One can see that the hadronic case seems to fit better concerning the calculated χ^2 and spectrum itself. The extra data taken into account is from the Fermi[6] observation in GeV range. Further information about the data used from Fermi can be found in [24]. Additionally PSR and PWN flux points taken from [[21], p.5] are plotted in the keV region as well as a flux point observed by the Australia Telescope Compact Array (ATCA) in the µeV energy band (see [22], p.2). For the data taken from Chandra observations only an energy band of 0.5-7keV was given, such that the energy axis point of the flux points shown in the plots is the mean value of 3.25keV. Chandra also observed both the SNR and PWN. Hence the reason that both cases are possible for this source, like one can see in figures 8 and 9. The flux points in the µeV-keV energy band are taken from [[30], p.14] and were specifically determined for the PWN.

model	name	value	unit
power law	α	2.5	
power law	E_{total}	$4\cdot10^{50}$	erg
log parabola	α	2.5	
log parabola	β	0.8	
log parabola	E_{total}	10^{47}	erg
pp interaction	ambient density	40	cm^{-3}
synchrotron	B field	27	µG

Table 3: Particle injection model parameters for the hadronic case.

---

[6]Data taken from the 3FGl catalog, which can be found on the website `https://fermi.gsfc.nasa.gov/ssc/data/access/lat/4yr_catalog/`
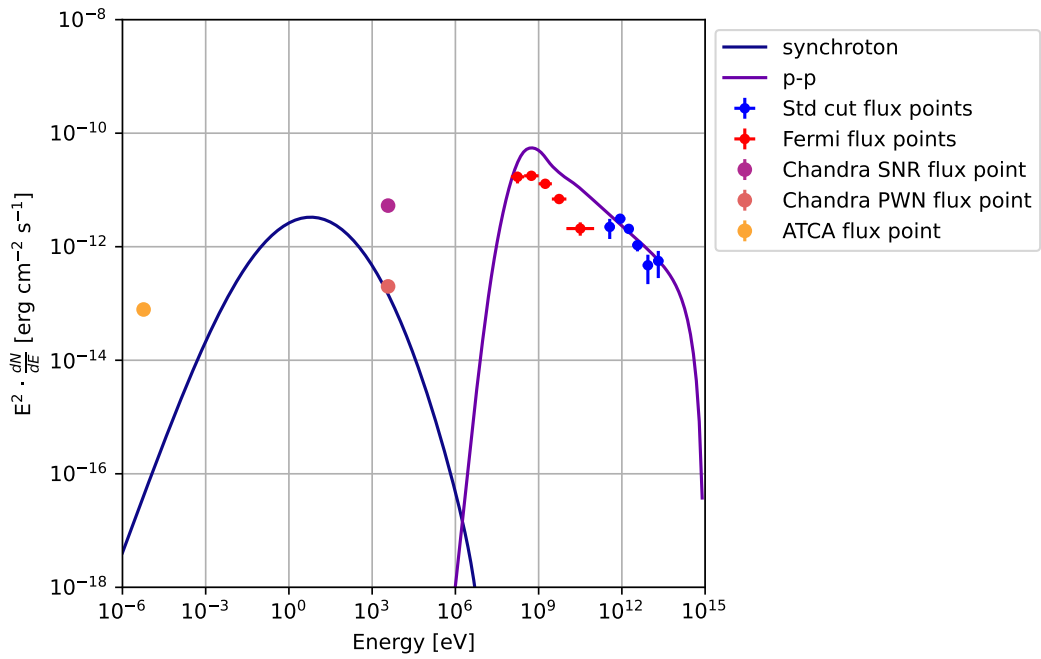
Figure 8: Total SED for hadronic emission together with the synchrotron emission. For this case a seperate leptonic model is used as a leptonic emission is better describable by a logarithmic injection spectrum.
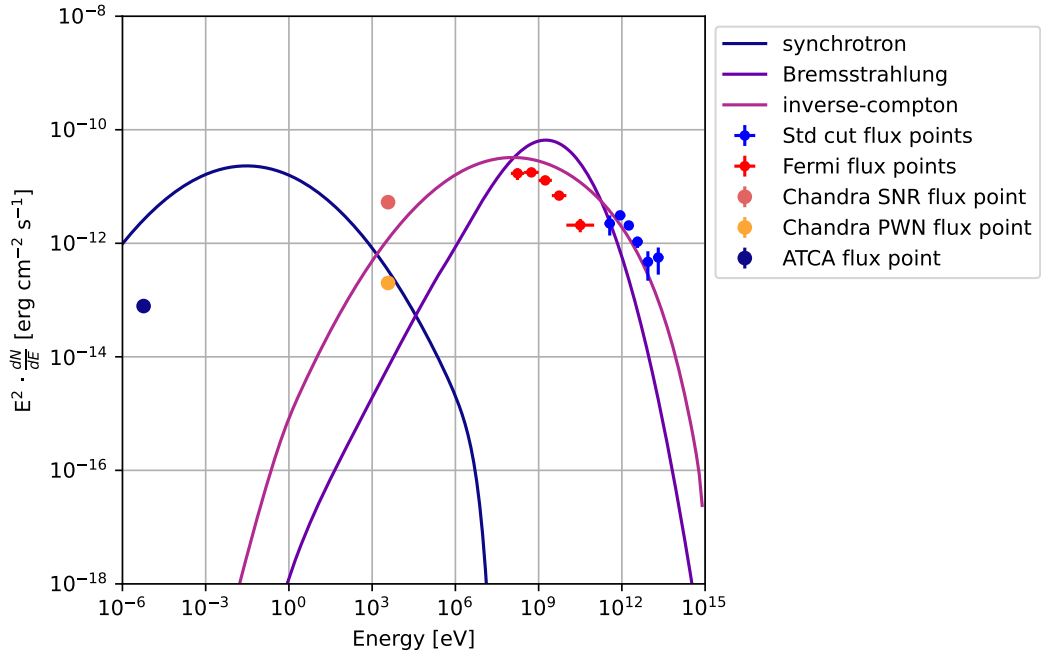
Figure 9: Total SED for leptonic emission with a synchrotron emission described by the same logarithmic injection spectrum as the inverse compton spectrum.

model	name	value	unit
log parabola	α	3.5	
log parabola	β	0.3	
log parabola	E_{total}	$5 \cdot 10^{49}$	erg
synchrotron	B field	27	μG
photon field	temperature	2.7	K
photon filed	energy density	25	eV cm^{-3}
bremsstrahlung	ambient density	40	cm^{-3}

Table 4: Particle injection model parameters for the leptonic case.

Regarding the total energy range both models could fit to the obtained data points. This means that the hadronic origin of the gamma-rays in a broad band measurement is as likely as the leptonic one. Taking [[17], p.25] into account, for a pulsar with spin down luminosity of $\sim 10^{36}$ergs^{-1} a magnetic field between 25-35μG is likely. In this case a magnetic field of 27μG is taken for both models. In both cases Fermi data has an offset to the models which can not be neglected, resulting in the model curve to be slightly above the data points in the GeV energy range. Concerning the low energy band, both models do not fit to the data from ATCA. Taking this into account, no final decision between leptonic and hadronic emission can be made. However an argument for the hadronic case is that the efficiency $\epsilon_{1-10\text{TeV}}$ found is more likely belonging to a PWN than a SNR. In addition the best fit spatial model location is within error assumptions identical with the PWN. An argument for the composite system is that even though both the hadronic and leptonic model fit to the VHE flux points,

the hadronic emission model seems to fit better. However as both leptonic and hadronic injection loss spectra could fit for this source, the status of being a composite source stays.

4.2 HESS J1833-105

HESS J1833-105 is around 870 years old and is like HESS J1119-614 a composite system [[28], p.5]. It lies in a distance of around 4.8kpc and has spin-down luminosity of $\dot{E} \approx 3.4 \cdot 10^{37} \mathrm{ergs}^{-1}$ [[16], p.40]. The total live time data was taken is around 56.08 hours, the mean zenith angle for the 124 data runs is around 22.46°, whereas the mean offset is around 1.21°. Again the average live time of each observation run is around 28min. A histogram with all zenith and offset angles is depicted in figure 10. The distribution of standard and hard cut are again the same. It is decided to use the hard cut for further analysis as it turns out to be best fitting
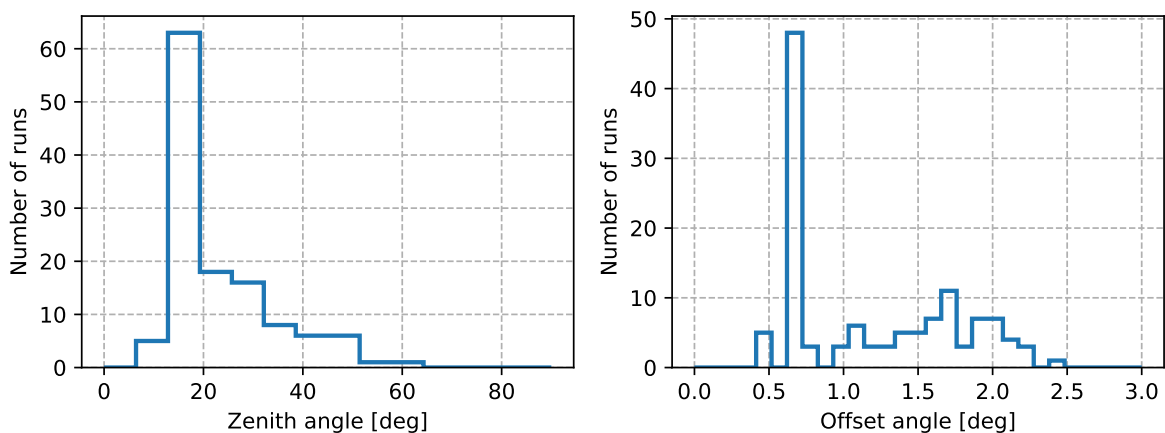

Figure 10: Zenith and offset angle distribution for HESS J1833-105. Note that in this case most of the runs have an offset between 0.5°-1.0°, as there is a high peak.

to the calculated model from HGPS.

4.2.1 Data analysis & Modeling

The hard cut data now has less total counts and thereby also less background and excess counts in general when compared to standard cut data. The corresponding off region significance histogram can be seen in figure 11, where in this case the off region cut on the right flank is softer. The shape of the excluded region for the background reduction has a normal distribution shape, which means that no gamma-ray emission belonging to the source is cut out. Yet one can argue that maybe a couple of the background emission counts are contained in this source, as the right flank of the off graph has a little plateau, which indicates that this data should acutally belong to the background. However as this makes up only a smaller portion of the histogram and still a reasonable amount of the all bin histogram can be seen. With this taken into account no significant contamination regarding the signal to background differentation occurs, such that the data can be safely taken for further usage. Also a larger energy threshold of (0.60±0.23)TeV is retrieved from the IRF comparison, which is expected for hard cut data. From 13687 only 553.80 are belonging to the source, which means 13133.2 are background counts, which makes up a signal to background ratio of
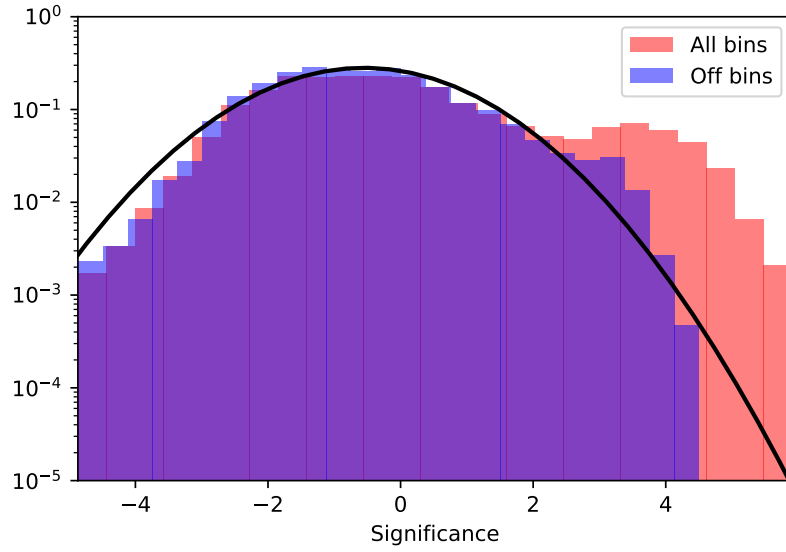
Figure 11: Off region histogram obtained after the background reduction. Note that less counts belonging to the background can be observed, indicating that some gamma-ray emission belong to a seperate source, which is not excluded is taken falsely into account.

4.0%. The comparison plot of both spectral fits with HGPS data can be seen in figure 12. A percental flux of (2.4±0.2)% for power law fit data and (2.0 ±0.3)% for exponential fit data in Crab units is computed in this case. Here the exponential cutoff fit gives a closer value to the one computed by HGPS. The fit parameters are shown in tables 5 and 6, where in both cases an error for sigma which is at least as big as the value itself is found. Both have a circular shape and only the upper limit of 0.03° can be obtained for this source. As both images thereby look the same, it is decided to only plot one of them. This sky map alongside the containment radius can be seen in figure 13.
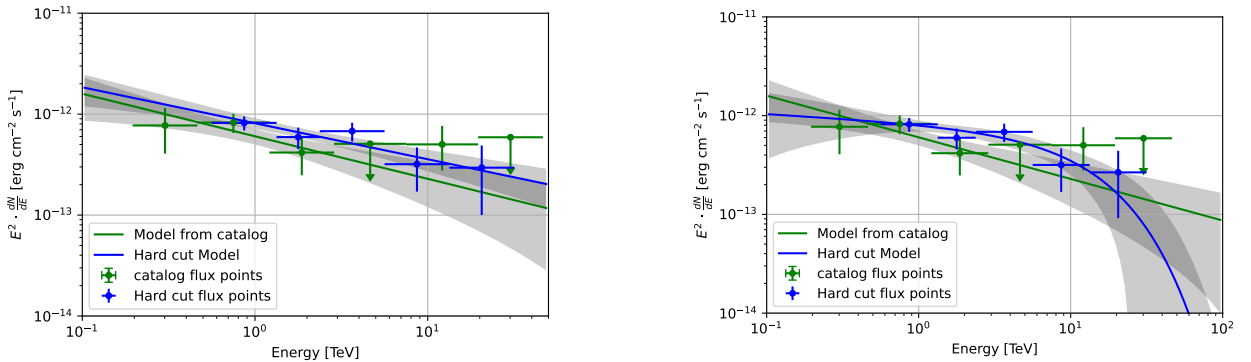

Figure 12: Hard cut spectral models in comparison with HGPS models. Note that less flux points are obtained in this case.

Another reason why hard cut data is used in this case, is that the $\sqrt{TS}$ value for the sky map is higher for this cut, than for standard cut data. This means that the counts from this cut have a higher significance than for the other, making it more reasonable to use it.

type	parameter	value	unit
spatial	R.A. (J2000)	278.40 ± 0.003	deg
spatial	Dec. (J2000)	-10.57 ± 0.005	deg
spatial	σ	0.003 ± 0.003	deg
spectral	ϕ	$(5.068 \pm 0.640) \cdot 10^{-13}$	$\mathrm{TeV^{-1}cm^{-2}s^{-1}}$
spectral	Γ	2.357 ± 0.119	

Table 5: Fit values for the power law fit with errors. In comparison with table 6, the amplitude ϕ and spectral index Γ have smaller error values.

type	parameter	value	unit
spatial	R.A. (J2000)	278.39 ± 0.003	deg
spatial	Dec. (J2000)	-10.573 ± 0.005	deg
spatial	σ	0.003 ± 0.005	deg
spectral	ϕ	$(5.297 \pm 0.720) \cdot 10^{-13}$	$\mathrm{TeV^{-1}cm^{-2}s^{-1}}$
spectral	Γ	2.089 ± 0.270	
spectral	λ	0.068 ± 0.068	$\mathrm{TeV^{-1}}$
spectral	α	1.000 ± 0.000	

Table 6: Fit values for exponential cutoff fit with errors. The error for σ is in this case even bigger than the value itself.
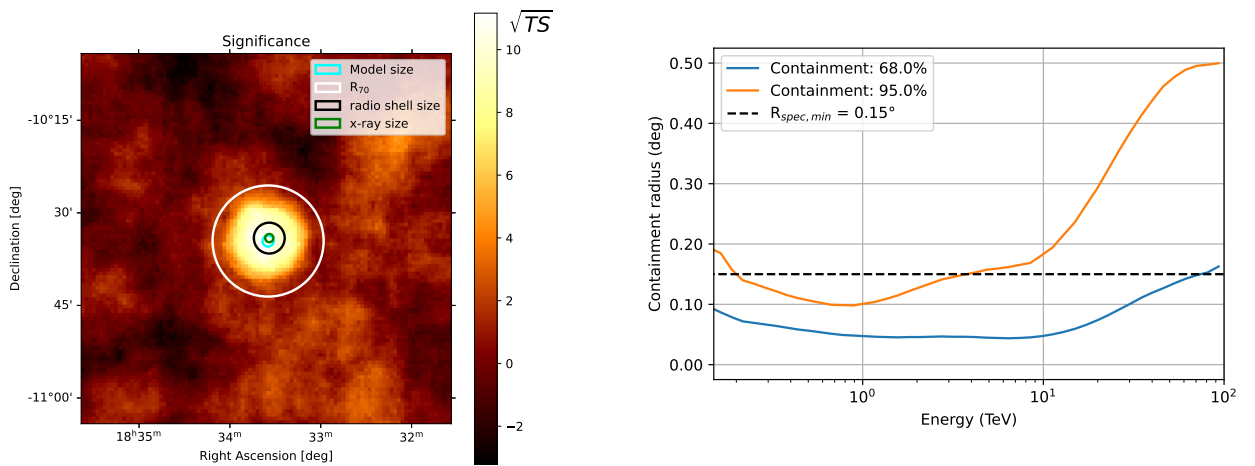

Figure 13: Sky map and containment radius for the hard cut data. Note that the containment radius energy range has a lower limit 0.15TeV set on. The FOV for the sky map is 1°×1° and the X-ray size is almost as big as the obtained model size.

4.2.2 Interpretation

It turns out that the power law fit flux points actually have a slightly lower $\sqrt{TS}$ value than the exponential cutoff flux points ($\sqrt{TS}_{\text{exp}} = 6.18 > \sqrt{TS}_{\text{pwl}} = 6.17$). However as this difference is neglectable within error assumptions, the basis for decision-making are the errors of the amplitude and spectral index. They are smaller in the power law case, which makes them the more optimal choice to describe the source.

Using equation 11, a luminosity of $(3.37 \pm 0.40) \cdot 10^{33} (d/4.8\text{kpc})^2$ ergs^{-1} is calculated, which results in a gamma ray conversion efficieny of $\epsilon_{1-10\text{TeV}} = 0.01\%$. This value is again below the 10% range defined by [18]. For HESS J1833-105 no braking index is known, such that n=3 is assumed. Using $\tau_0 = 1$kyr and the estimated age of 870yr the current pulsar energy E(t)=$1.74 \cdot 10^{48}$erg is found. The best fitting model has a χ^2 value of 0.12 for the hadronic and 0.06 for the leptonic case and is thereby valid in both cases (with 4 d.o.f.). The model parameters are listed in tables 6 and 7. Hadronic and leptonic models are shown in figures 14 and 15, where the hadronic case fits better to the total SED case. Fermi flux points are taken from their already mentioned catalog. The extra X-ray observation data is from by Chandra, Hitomi and Nustar and the infrared from Herschel and Spitzer (see [30] for a more detailed explanation of the data acquisition, as well as further information on the flux points). Both the X-ray and infrared flux points are from [[30], p.15]. In the hadronic case a magnetic field of 32µG is used, which suits to the values obtained by [[17], p.25], which lie between 35-70µG. For the leptonic case a B-field of 200µG turns out to be best fitting, making it more unlikely to describe the broad band emission. Note that in the latter case one global injection model on the basis of equation 18 is used, whereas for the hadronic model two seperate models are used.
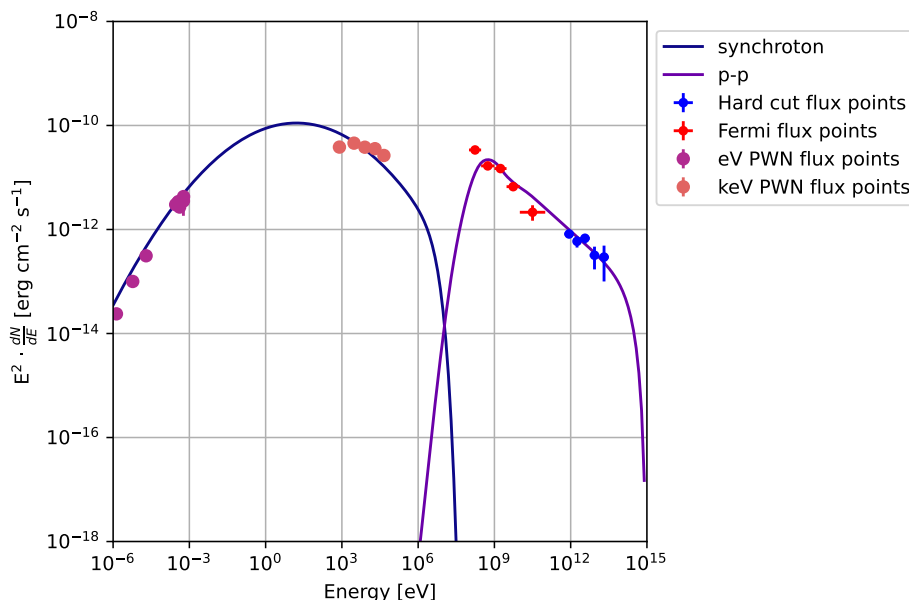

Figure 14: Total SED for hadronic interaction model with additional data points with keV data taken from Fermi. Additionally the radio and X-ray PWN points are taken from [[30], p.15], where further information about the data and where it was taken is given.

However for HESS J1833-105 the hadronic model tends to fit better, than the leptonic one.

Regarding the flux points from Fermi not all are fitting perfectly on the curve, but this is acceptable within the error range. Additionally the flux from [[30], p.15] are all PWN data points, making the hadronic case together with the B-field considerations more likely. However taking only VHE emission into account and considering that Fermi determined the source for this emission to be from a PSR, a definitive decision is not possible. Yet looking at the broad band spectrum a hadronic emission is more likely than leptonic interactions. Besides that no significant divergence between the spatial model location and the PWN location occurs. It is remarkable that the hadronic emission model tends to fit better, even though a PWN emission normally belongs to the leptonic emission case. Hoewever as the data fits better for the hadronic injection model, this seems to be within error assumptions the better fitting model. In summary, neither critical arguments against the composite system nor convincing data obtained from this analysis for the PWN system can be found. This makes the status of HESS J1833-105 as being a composite system still the most possible option, even though much evidence points towards a PWN.
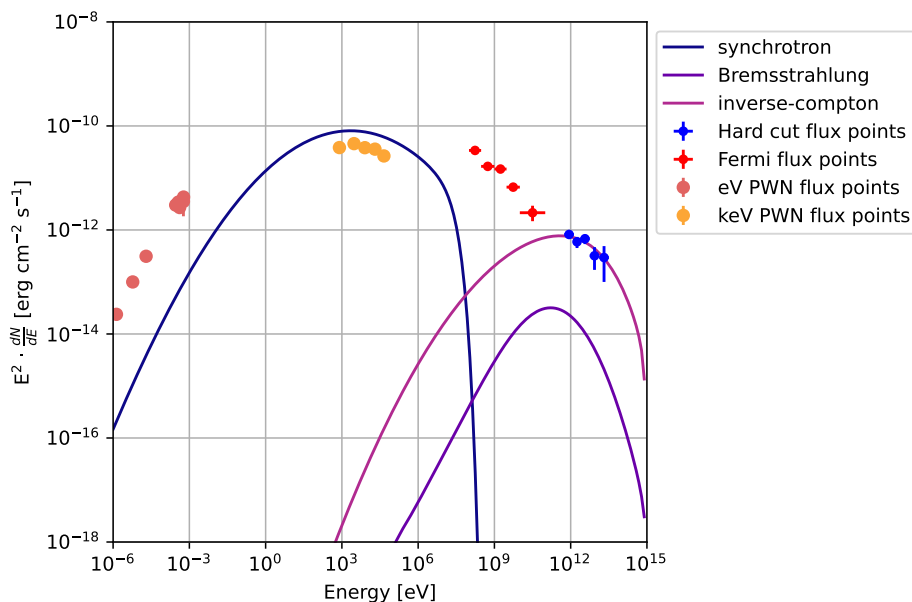

Figure 15: Total SED for leptonic model with a smaller Bremmstrahlung interaction curve than for the SED from HESS J1119-614.

model	name	value	unit
power law	α	2.5	
power law	E_{total}	10^{50}	erg
log parabola	α	2.7	
log parabola	β	0.3	
log parabola	E_{total}	$2.5 \cdot 10^{48}$	erg
pp interaction	ambient density	20	cm^{-3}
synchrotron	B field	32	μG

Table 7: Particle injection model parameters for the hadronic case.

model	name	value	unit
log parabola	α	2.3	
log parabola	β	0.3	
log parabola	E_{total}	10^{46}	erg
synchrotron	B field	200	μG
photon field	temperature	2	K
photon filed	energy density	10	eV cm^{-3}
bremsstrahlung	ambient density	20	cm^{-3}

Table 8: Particle injection model parameters for the leptonic case.

4.3 HESS J1846-029

The last source reanalysed is HESS J1846-029, which has a high magnetic surface field of $4.9 \cdot 10^{13}$G [[31], p.1] and lies in an estimated distance of around 6kpc [[16], 42]. Alongside that it is one of the youngest systems to be observed with an estimated age of 723yr. Its pulsar has a spin-down Lumiosity $\dot{E} = 8.3 \cdot 10^{36}$ergs^{-1}[[16], p.41], which is the lowest of the three sources, although it is the youngest observed source. For the analysis of this source a total live time of 69.63 hours is taken and a total number of 151 observation runs are considered in this analysis. The average live time of each run is about 28min. Furthermore a mean zenith angle of 29.70° with an average offset of 1.26° occurs in this case, see figure 16 for a histogram of these values. Standard and hard cut have the selfsame observation angle distribution. Again the usage of standard cut data turns out to be the more favorable one,
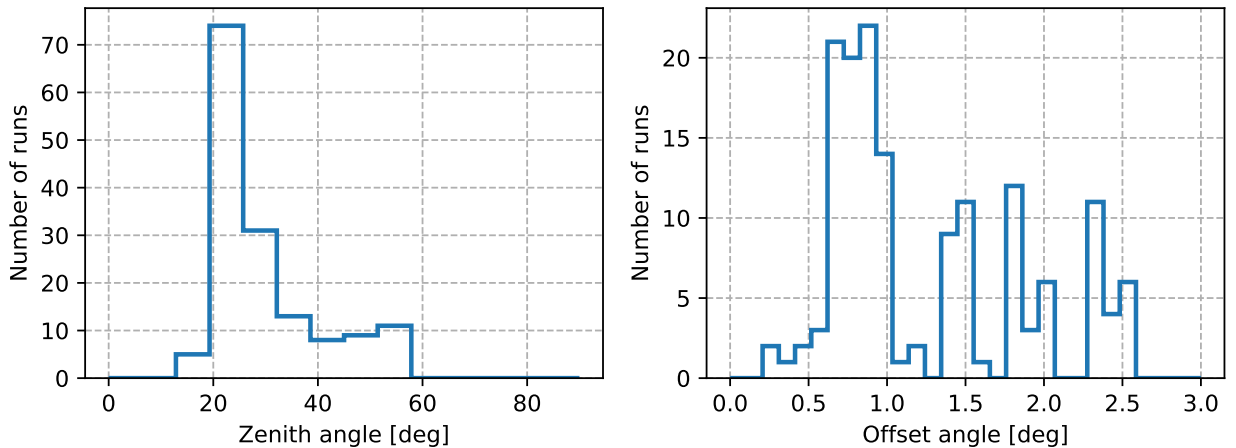

Figure 16: Zenith and offset angle histogram for HESS J1846-029. Note that the offset angle distribution resembles the distribution HESS J1119-614 has had.

as the flux point estimation turns out to be less valid for hard cut data.

4.3.1 Data analysis & Modeling

For the standard cut an average energy threshold of (0.40±0.16)TeV is applied on the data. This results in a reduction, where only 3806.07 of 39271 total counts belong to the source

excess. This makes up a source to background count ratio of 10.73%, which is way higher than the values obtained before. The significance histogram in figure 17 shows the off region, which like before is the excluded region for background calculations. The shape of the off region histogram is a normal distribution, which is in this case much smaller than the histogramm with all counts taken into account. The reason for this is that there are two other sources in the direct neighborhood of HESS J1846-029, these being HESS J1843-033 and a not yet classified gamma-ray emission region, called HOTS J1845-026[7]. The calculated spectral
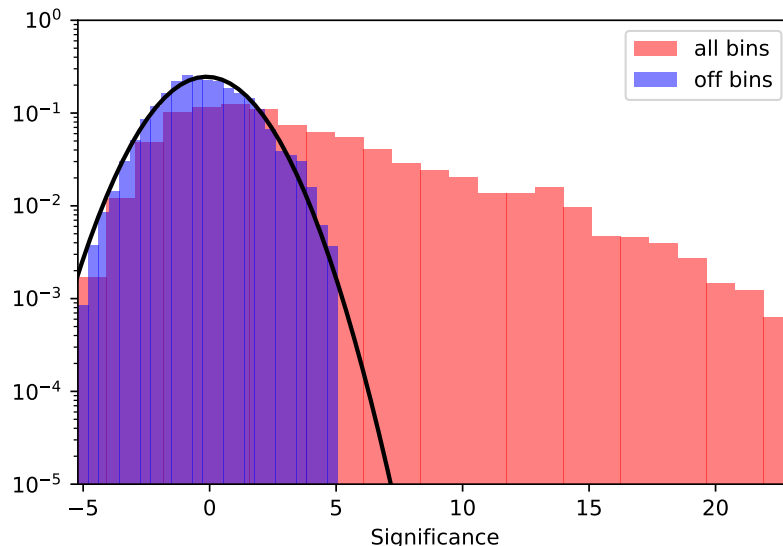

Figure 17: Significance histogram obtained after the background reduction is applied, with the excluded region counts (blue) and all counts (red) taken into account.

models can be seen in figure 18, with the fit parameters can be seen in tables 9 and 10. A percental crab units flux of (2.4±0.2)% for power law data and (1.5±0.2)% for exponential cutoff data is found. In this case exponential cutoff data fits better to the percental flux calculated by [[32], p.3], where a flux of ∼2% is obtained. Yet again for higher energies the HGPS spectral model and the exponential cutoff do not overlap, whereas the power law does. This however can be explained by the fact that HGPS also uses a power law. Considering

type	parameter	value	unit
spatial	R.A. (J2000)	281.60 ± 0.0003	deg
spatial	Dec. (J2000)	-2.976 ± 0.0001	deg
spatial	σ	0.0004 ± 0.0001	deg
spectral	ϕ	$(5.740\pm0.496)\cdot10^{-13}$	$TeV^{-1}cm^{-2}s^{-1}$
spectral	Γ	2.483 ± 0.077	

Table 9: Fit values for the power law fit with errors.

---

[7]It is not knwon how the gamma-ray emission is produced from HOTS J1845-026, which further experiments and observations could change.
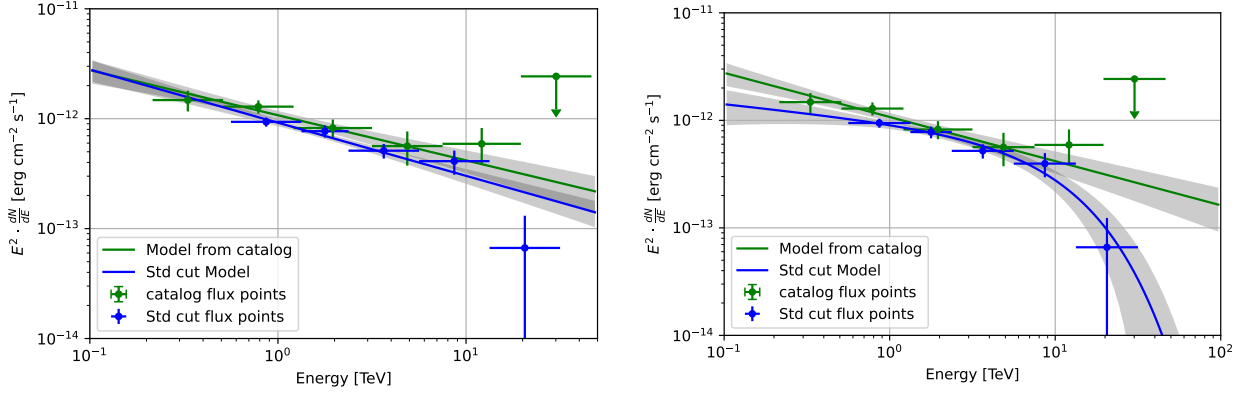
Figure 18: Power Law (left) and exponential cutoff (right) fit with HGPS data and model. Note that in both cases five flux points could be obtained, which in both cases fit well to HGPS data from their catalog.

type	parameter	value	unit
spatial	R.A. (J2000)	281.60 ± 0.002	deg
spatial	Dec. (J2000)	-2.977 ± 0.003	deg
spatial	σ	0.002 ± 0.003	deg
spectral	ϕ	$(6.314 \pm 0.387) \cdot 10^{-13}$	$TeV^{-1}cm^{-2}s^{-1}$
spectral	Γ	2.161 ± 0.155	
spectral	λ	0.090 ± 0.046	TeV^{-1}
spectral	α	1.000 ± 0.000	

Table 10: Fit values for exponential cutoff power law fit with errors. The resulting value for σ has a larger error than the value itself.

the spatial dimensions for both fits the upper size limit needs to be applied. Thereby the source size is 0.03° for this cut, a resulting image of the source alongside its containment radius can be seen in figure 19. Again only one sky image is shown, because both fits have the same size. A containment radius of the fix value of 0.15° is again obtained in this case. The radio and gamma-ray sizes are both taken from [[33], p.1]. One can see that the source size more or less lies between the radio and gamma-ray shell size. Additionally the found model location coordinates from our source models lie within the error range on the same spot as the PWN.
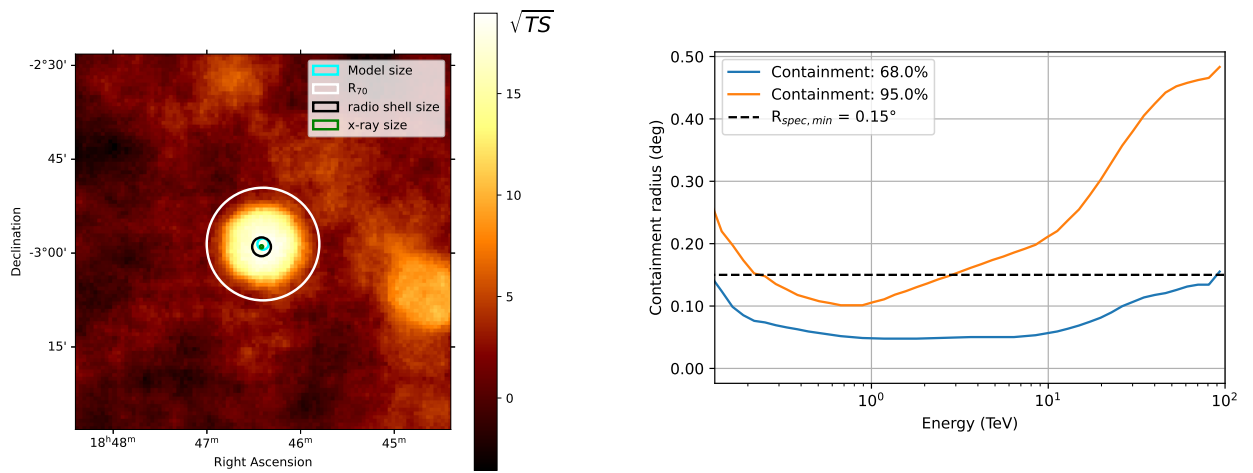
Figure 19: Sky map and containment radius for hard cut data. The FOV for the sky map is 1°×1°.

4.3.2 Interpretation

Concerning the $\sqrt{TS}$ value for the flux point estimation the decision to use the power law is made as it has a higher value (6.22 (power law) compared to 6.17 (exponential cutoff)). The resulting luminosity is $(5.54 \pm 0.54) \cdot 10^{33} (d/_{6\text{kpc}})^2$ ergs^{-1}, which makes up a conversion effeciency of $\epsilon_{1-10\text{TeV}}$=0.07%, which is comparable to the HPGS value of 0.08% [see [16], p.42]. This also indicates that the observed spectrum is likely to be because of a PWN. Additionally the pulsar energy of E(t)=3.24$\cdot10^{47}$erg for the estimated age of 723yr, n=3 and τ_0=1kyr is found. This makes HESS J1846-029 the least energetic system to be observed, even though it is the youngest.

A caveat in this case concerning the hadronic/leptonic classification is that for this system no data in the GeV energy range has been taken to this date. Hence the reason that both cases are possible for this source, like one can see in figures 20 and 21. The additional data points used in the keV band are obtained from [[31], p.5]. There only the energy band is mentioned for which the flux points were obtained, such that the mean value of this band is used to plot the points. Additionally μeV data from [[34], p.433] is taken into account, who identified the emission in this energy band to be from a composite system.
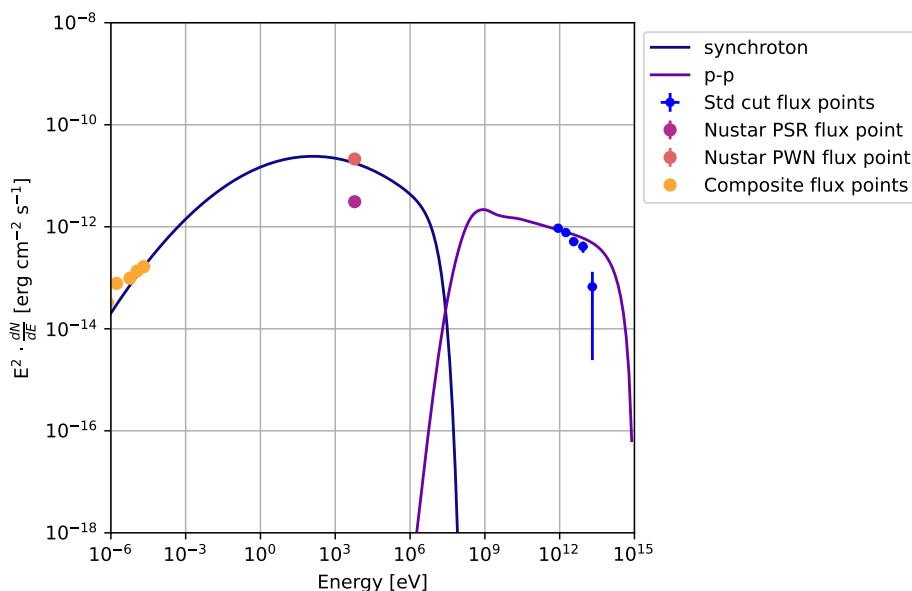

Figure 20: Total SED for hadronic model with B=80μG, which is the best fitting model concerning the brad band SED.

In the hadronic case a χ^2 value of 7.25 and for leptonic one 6.69 is calculated making both viable models (for 4 d.o.f.). The fit parameters can be seen in tables 11 and 12. It is notable that the magnetic field used in the hadronic case has a much smaller value than the leptonic one. Considering [[17], p.25] the hadronic magnetic field value fits better to their obtained magnetic field range.

Furthermore the synchrotron emission is fitted such that it merges the PWN keV flux point.

model	name	value	unit
power law	α	2.2	
power law	E_{total}	$2.5{\cdot}10^{49}$	erg
log parabola	α	2.7	
log parabola	β	0.2	
log parabola	E_{total}	$2.5{\cdot}10^{47}$	erg
pp interaction	ambient density	17	cm^{-3}
synchrotron	B field	35	µG

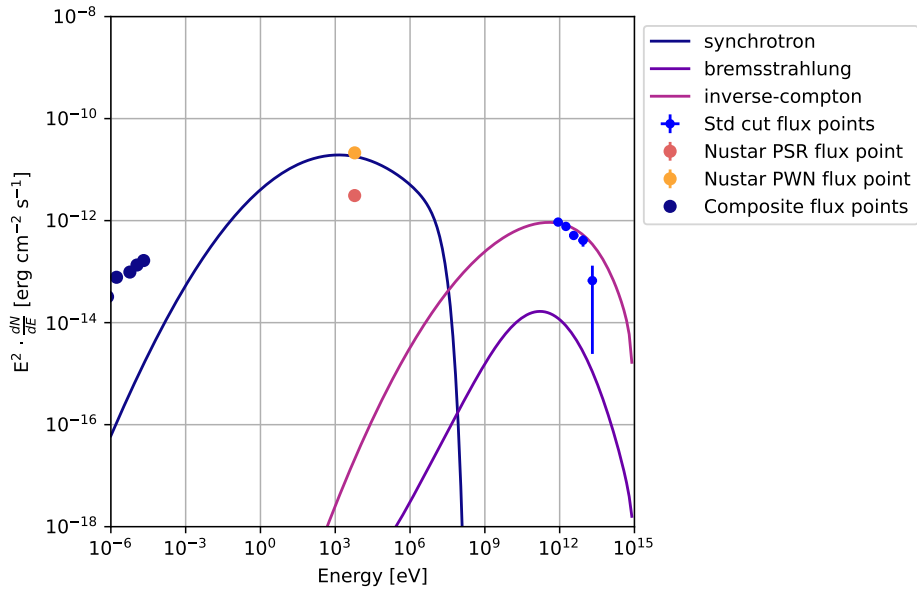Table 11: Particle injection model parameters for the best fitting hadronic case.

Figure 21: Total SED for leptonic model with B=125µG, which is the best fitting leptonic model, but not the best fitting considering the broad band energy.

model	name	value	unit
log parabola	α	2.3	
log parabola	β	0.3	
log parabola	E_{total}	$6{\cdot}10^{46}$	erg
synchrotron	B field	125	µG
photon field	temperature	2	K
photon filed	energy density	20	eV cm^{-3}
bremsstrahlung	ambient density	17	cm^{-3}

Table 12: Particle injection model parameters for the best fitting leptonic case.

It turns out that a PWN origin of the μeV-keV band is more favorable, as a fit through the PSR flux point results in a miss match of the fit curve in the μeV energy band for both cases (see figures 22 & 23). There the selfsame model parameters as for the found models are used, however a different magnetic field is applied. Yet analysing only VHE gamma-rays no decision can be made conerning the source kind. Further measurements in the GeV range need to be done in order to see the shape of the whole energy spectrum. Although the obtained conversion efficiency indicates that a PWN origin is more favorable. In conclusion with the VHE gamma-rays from HESS J1846-029 that are obtained no decision between SNR or the PWN can be made, such that the composite model status stays. However concerning the broad band flux a PWN origin seems to be more favorable.
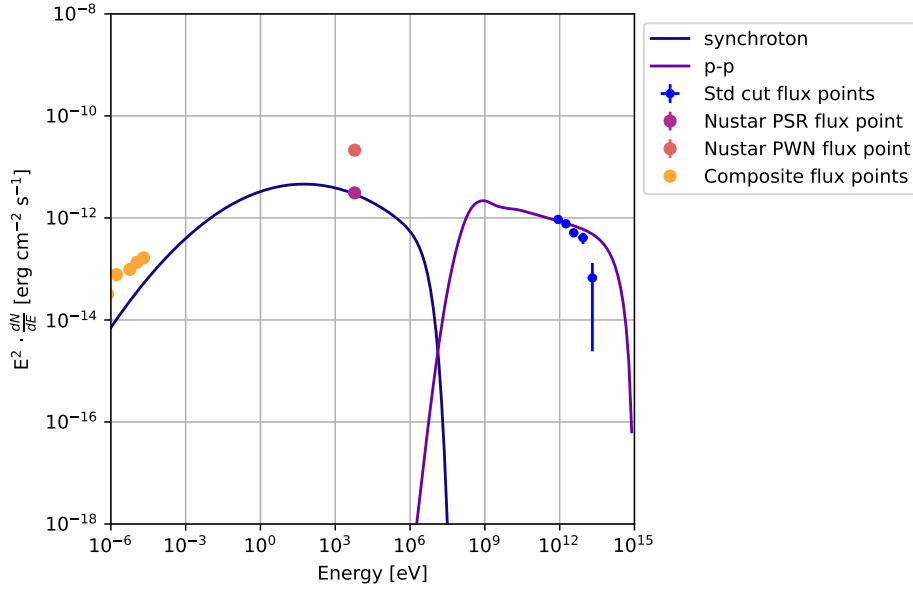

Figure 22: Total SED for hadronic model with a magnetic field of 35μG. The synchrotron field is fitted on the PSR flux point in this instance.
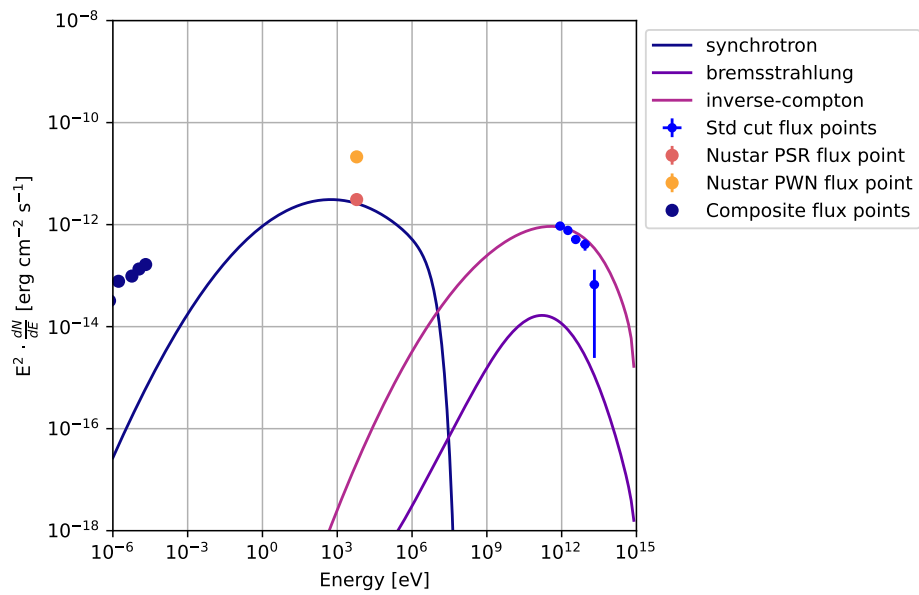
Figure 23: Total SED for leptonic model with a synchrotron model fixed to be going through the PSR flux point with a B-field of 50μG.

5 Summary

The three sources HESS J119-614, HESS J1833-105, HESS J1846-029 have been reanalysed in their VHE energy band. The data used was taken from H.E.S.S telescope array during phase one of its existence. For all data sets the individual instrument response function was considered in the data selection, such that a standard and hard cut were defined. The first one used more optimistic cuts than the second one, when concerning the bias of the energy, which was in all cases set to be 10% of the maximum energy measured. For both cases several background reduction calculations were applied taking the instrument response function parameters of each observation run into account. The energy cut for hard cut data thereby turned out to be higher than the standard cut data. Onto the stacked data sets, fits were performed, including a gaussian spatial model and a simple power law, as well as an exponential cutoff power law for spectral properties. With these models set on, flux points were calculated in the energy range from 0.1-30TeV. These were then compared to HGPS data in order to ensure a reasonable calculation of the flux. In addition sky maps including the radio shell and X-ray emission shell size was plotted alongside the 70% containment radius retrieved from the PSF. Finally a decision for the best fitting model in spatial and spectral model was made. This resulted in the usage of power law flux points for all three sources, where for HESS J1119-614 and HESS J1846-029 standard cuts and for HESS J1833-105 hard cuts were used. After that the Luminosity and conversion efficiency were calculated, which confirmed the values obtained by HGPS. Also the estimated energy of the system was calculated, where HESS J1846-029 turned out to have the smallest energy, even though it is the youngest of the three analysed systems. At last a hadronic and leptonic model was applied to the flux points, using a 5% significance χ^2 test. For HESS J1119-614 a composite model is still the best description for VHE data. For HESS J1833-105 a hadronic model seems to be the most likely when looking at the total SED. This however only holds in broad band considerations, whereas for the VHE emission alone no decision could be made. For HESS J1846-029 no decision could be made either as in this case no identified corresponding source is found until now. This resulted in deciding that this source also can not be categorised as either a hadronic or leptonic energy emission source. In conclusion no definitive categorisation in all three cases could be made, such that the status of being composite SNR and PWN systems still holds. However results from this analysis suggest that VHE emission is more likely to be from PWN in all three cases. A reason for that is the conversion efficiency, which in all three cases out to be less than 10% and thereby being in the efficiency range in which PWN are likely to find.

References

[1] NASA HEASARC, "Introduction to Supernova Remnants.", *NASA*, 11.05.2011, `https://heasarc.gsfc.nasa.gov/docs/objects/snrs/snrstext.html`. Accessed: 04.07.2022, 4:31pm.

[2] Abdalla, H., et al. "Particle transport within the pulsar wind nebula HESS J1825–137." Astronomy & Astrophysics, vol.621, A116 (2019).

[3] Klingler, Noel, et al. "The Mouse Pulsar Wind Nebula." The Astrophysical Journal, vol.861, No.1 (2018).

[4] NIST, "What is synchrotron radiation?", *NIST*, 02.06.2021, `https://www.nist.gov/pml/sensor-science/what-synchrotron-radiation`. Accessed: 18.07.2022, 1:44pm.

[5] Williams, Oliver, *UCLA PBPL-Inverse Compton Scattering*, Winter 2003, `http://pbpl.physics.ucla.edu/Education/Courses/Physics_199/Inverse_Compton/`. Accessed: 18.07.2022, 2:13pm.

[6] Connor, Nick, *What is Bremsstrahlung–Definition*, 14.12.2019, `https://www.radiation-dosimetry.org/what-is-bremsstrahlung-definition/`. Accessed: 18.07.2022, 2:21pm.

[7] Türler, Marc, *Supernova remnants accelerate cosmic rays*, 28.03.2013, `https://cerncourier.com/a/supernova-remnants-accelerate-cosmic-rays/`. Accessed: 18.07.2022, 4:48pm.

[8] Hofmann, W., "The H.E.S.S Telescopes.",*H.E.S.S.-The High Energy Stereoscopic System*, 2012, `https://www.mpi-hd.mpg.de/hfm/HESS/pages/about/telescopes/`. Accessed: 27.06.2022, 2:36pm.

[9] Harvard-Smithsonian Center for Astrophysics, "Pulsar wind nebulae.", *Phys.org*, 07.11.2016, `https://phys.org/news/2016-11-pulsar-nebulae.html`. Accessed: 04.07.2022, 5:33pm.

[10] Gammapy project, "Data access and selection (DL3).", *Data access and selection (DL3)-gammapy v0.20*, 2017, `https://docs.gammapy.org/0.20/userguide/dl3.html`. Accessed: 05.07.2022, 07:22am.

[11] Gammapy project, "IRF Theory.", *IRF Theory-gammapy v0.20*, 2017, `https://docs.gammapy.org/0.20/irf/theory.html#irf-theory`. Accessed: 05.07.2022, 07:26am.

[12] Deil, Christoph, et al. "Gammapy-A prototype for the CTA science tools." (2017).

[13] Donath, Axel, et al. Gammapy: Python Toolbox for Gamma-ray Astronomy. v0.20, Zenodo, 13 May 2022, doi:10.5281/zenodo.6552377.

[14] Gammapy project, "Gaussian spatial model.", *Gaussian spatial model-gammapy v0.20*, 2017, `https://docs.gammapy.org/0.20/modeling/gallery/spatial/plot_gauss.html?highlight=gaussian`. Accessed: 05.07.2022, 11:32am.

[15] Atoyan, A. M., and F. A. Aharonian. "Modelling of the non-thermal flares in the Galactic microquasar GRS 1915+ 105." Monthly Notices of the Royal Astronomical Society, vol.302, No.2 (1999).

[16] H.E.S.S. Collaboration, Abdalla, H., Abramowski, A., et al. "The HESS Galactic plane survey." Astronomy & Astrophysics, 612, A1 (2018).

[17] Conrad, J.M., et al. "The population of TeV pulsar wind nebulae in the HESS Galactic Plane Survey." Astronomy and Astrophysics, 612 (2018).

[18] Kargaltsev, Oleg, Blagoy Rangelov, and George G. Pavlov. "Gamma-ray and X-ray properties of pulsar wind nebulae and unidentified Galactic TeV sources." (2013).

[19] Hahn, Joachim, Carlo Romoli, and Mischa Breuhaus. "GAMERA: Source modeling in gamma astronomy." Astrophysics Source Code Library (2022): ascl-2203.

[20] Kumar, Harsha S., Samar Safi-Harb, and Marjorie E. Gonzalez. "Chandra and XMM-Newton studies of the supernova remnant G292. 2–0.5 associated with the pulsar J1119–6127." The Astrophysical Journal, 754, No.2 (2012).

[21] Blumer, Harsha, et al. "Back to Quiescence: Postoutburst Evolution of the Pulsar J1119–6127 and Its Wind Nebula." The Astrophysical Journal, 917, No.2 (2021).

[22] Crawford, Fronefield, et al. "A Radio Supernova Remnant Associated with the Young Pulsar J1119–6127." The Astrophysical Journal, vol.554, No.1 (2001).

[23] Gammapy project, "Estimators (DL4 to DL5, and DL6)", *Estimators (DL4 to DL5, and DL6)-gammapy v0.20*, 2017, `https://docs.gammapy.org/0.20/userguide/estimators.html`. Accessed: 05.07.2022, 8:35pm

[24] Acero, Fabio, et al. "Fermi large area telescope third source catalog." The Astrophysical Journal Supplement Series, vol.218, No.2 (2015).

[25] Gammapy project, "Source code for gammapy.modeling.models.spatial", *gammapy.modeling.models.spatial-gammapy v0.20*, 2017, `https://docs.gammapy.org/0.20/_modules/gammapy/modeling/models/spatial.html#GaussianSpatialModel.to_region`. Accessed: 06.07.2022, 12:45pm.

[26] Pierce, Rod. "Chi-Square Table", *Math Is Fun*, 26.04.2022, `http://www.mathsisfun.com/data/chi-square-table.html`. Accessed: 06.07.2022, 3:16pm.

[27] Popescu, C. C., et al. "A radiation transfer model for the Milky Way: I. Radiation fields and application to high-energy astrophysics." Monthly Notices of the Royal Astronomical Society, vol.470, No.3 (2017).

[28] Bietenholz, M. F., and N. Bartel. "The expansion and radio spectral index of G21. 5- 0.9: is PSR J1833- 1034 the youngest pulsar?." Monthly Notices of the Royal Astronomical Society, vol.386, No.3 (2008).

[29] Aharonian, Felix, et al. "Observations of the Crab nebula with HESS." Astronomy & Astrophysics, vol.457, No.3 (2006).

[30] Hattori, Soichiro, et al. "The Nonstandard Properties of a "Standard" PWN: Unveiling the Mysteries of PWN G21. 5–0.9 Using Its IR and X-Ray Emission." The Astrophysical Journal, vol.904, No.1 (2020).

[31] Gotthelf, E. V., et al. "X-Ray Spectroscopy of the Highly Magnetized Pulsar PSR J1846-0258, Its Wind Nebula, and Hosting Supernova Remnant Kes 75." The Astrophysical Journal, vol.908, No.2 (2021).

[32] Djannati-Ataï, A., et al. "New Companions for the lonely Crab? VHE emission from young pulsar wind nebulae revealed by HESS." International Cosmic Ray Conference, vol.2 (2008).

[33] Becker, Robert Howard, David J. Helfand, and A. E. Szymkowiak. "G29. 7-0.3: another supernova remnant with an identity crisis." The Astrophysical Journal 268 (1983).

[34] Becker, R. H., and M. R. Kundu. "High-resolution radio observations of three supernova remnants." The Astrophysical Journal, vol.204 (1976).

I hereby ensure that I wrote this thesis myself and that I only used the references that are mentioned.

_____